Journal of Materials Chemistry A

PAPER

View Article Online
View Journal | View Issue

Cite this: J. Mater. Chem. A, 2019, 7, 8384

Photocatalytic reforming of sugar and glucose into H_2 over functionalized graphene dots†

Van-Can Nguyen,[a] Nei-Jin Ke,[a] Le Duy Nam,[a] Ba-Son Nguyen,[ab] Yuan-Kai Xiao,[a] Yuh-Lang Lee[ac] and Hsisheng Teng*[acd]

Photocatalytic reforming of biomass into H_2 combined with its counterpart, photosynthesis, constitutes a sustainable carbon cycle that produces a clean solar fuel. This study reports the use of environmentally benign graphene-based photocatalysts to effectively reform sugar and glucose. We produce a catalyst consisting of sulfur and nitrogen codoped graphene oxide dots (SNGODs) by sequentially annealing graphite-derived graphene oxide with sulfur and ammonia, exfoliating the annealed product into dots, and autoclaving the dots in an ammonia solution. The codoping introduces quaternary nitrogen into the graphene basal plane to patch the vacancy defects and autoclaving creates a conjugation between nitrogen nonbonding states and the graphitic-π orbital by introducing peripheral amide and amino groups. These functionalization steps enlarge the electron resonance domain, narrowing the bandgap and inducing charge delocalization and separation. Here, SNGODs deposited with a Pt cocatalyst effectively catalyzed H_2 production from aqueous solutions of sugar and glucose under visible light irradiation for more than 80 h. The apparent quantum yields of reforming of sugar and glucose reach 11% and 7.4%, respectively, under 420 nm monochromatic irradiation. This pioneer study demonstrates the superiority of using carbon-based photocatalysts for biomass reforming and provides a structure-tuning strategy for enhancing the catalytic activity.

Received 15th December 2018
Accepted 2nd March 2019

DOI: 10.1039/c8ta12123k

rsc.li/materials-a

1. Introduction

In clean renewable energy resource research, photocatalytic H_2 production in an aqueous solution has received considerable attention.[1,2] Water splitting over a semiconductor photocatalyst by using solar energy to produce H_2 and O_2 has a high degree of sustainability.[3–5] However, the recombination of photo-generated electrons and holes or the back reactions of the products on the semiconductor surfaces results in inefficient photocatalytic H_2 generation.[6–8] Electron donors, such as triethanolamine, alcohols, sulfides, sulfites, organic acids, and hydrocarbons, are often used to restrain the recombination process and improve photocatalytic H_2 production.[9–14] Regarding the renewability of H_2 resources, photocatalytic reforming of biomass materials, such as glucose ($C_6H_{12}O_6$) and sugar (sucrose, $C_{12}H_{22}O_{11}$)—readily available from natural cellulose and starch, respectively—represents a promising counterpart to photosynthesis for achieving a sustainable carbon cycle that produces clean solar fuels (Scheme S1 of the ESI†).[3,15–25] Most studies have used TiO_2 as the photocatalyst for reforming glucose or sugar to produce H_2.[3,15–18,22,23,25] TiO_2 is sensitive only to UV light; this limits the applicability of solar light to this TiO_2 photocatalytic reforming process. Sulfides, such as $Cd_xZn_{1-x}S$,[19] $ZnIn_2S_4$,[20] and MoS_2/CdS,[26] were used as visible light-sensitive photocatalysts in photocatalytic reforming of glucose for H_2 production. However, sulfide catalysts are susceptible to oxidation and chemically unstable in the aqueous reforming system. Moreover, Cd-containing sulfides are environmentally detrimental and thus unsuitable for practical applications.[27,28] Visible light-sensitive $Bi_xY_{1-x}VO_4$ was used in the photocatalytic reforming of glucose, but its activity in H_2 production was limited by the reaction environment.[21,29] Carbon- or graphene-based photocatalysts, which are environmentally benign and sensitive to visible light, are considered ideal media for producing clean and renewable H_2. Performance of a carbon- or graphene-based photocatalyst in the reforming of glucose or sugar for H_2 production requires exploration.

Reaction (R1) presents a complete dehydrogenation reaction in stoichiometric terms for photocatalytic reforming of glucose in an aqueous solution in the absence of O_2,[3,22] *i.e.*,

$$C_6H_{12}O_6 + 6H_2O \rightarrow 12H_2 + 6CO_2 \quad (R1)$$

[a]Department of Chemical Engineering, National Cheng Kung University, Tainan 70101, Taiwan. E-mail: hteng@mail.ncku.edu.tw
[b]Research Center for Applied Sciences, Lac Hong University, Vietnam
[c]Hierarchical Green-Energy Materials (Hi-GEM) Research Center, National Cheng Kung University, Tainan 70101, Taiwan
[d]Center of Applied Nanomedicine, National Cheng Kung University, Tainan 70101, Taiwan

† Electronic supplementary information (ESI) available. See DOI: 10.1039/c8ta12123k

On completion of the reformation process, CO_2 is the expected carbon-containing end product. Both glucose and sugar have a ring configuration (Scheme 1a and b). Glucose reforming is initiated by ring-opening reactions, occurring mainly at the C-1 site of glucose (RHCOH, in which the "C" represents the C-1 site) because its hydroxyl end is prone to deprotonation and forms $RHCO^-$ in a basic environment.[3,30] Adsorption of $RHCO^-$ anions or RHCOH molecules on the catalyst surface is the rate-limiting step to initiate the reforming because the photogenerated holes either interact directly with the adsorbed $RHCO^-$ or indirectly with the adsorbed RHCOH through the hole-produced $^{\bullet}OH$ radicals.[3,20,22,30–34] The direct interaction route (between holes and adsorbed $RHCO^-$) is dominant in a basic environment.[35–38] Reactions to initiate the reforming involve photogenerated electrons and holes and conclude with the following reactions:

Electrons:

$$2H_2O + 2e^- \rightarrow H_2 + 2OH^- \quad (R2)$$

$$RHCOH + OH^- \rightarrow RHCO^- + H_2O \quad (R3)$$

Holes:

$$RHCO^- + 2h^+ + OH^- \rightarrow RC{=}O + H_2O \quad (R4)$$

Photogenerated electrons interact with water to produce H_2, and the holes interact with deprotonated glucose to produce gluconolactone (RC=O), which then proceeds with the process of ring opening on further oxidation to form small molecules, and eventually produces the end product CO_2. Considering the governing role of the adsorption mechanism, carbon- or graphene-based photocatalysts, which can be functionalized with –OH, $–NH_2$, and other groups to adsorb $RHCO^-$ anions or RHCOH molecules through hydrogen-bonding, are promising photosensitive media for catalyzing glucose or sugar reforming (Scheme 1c).

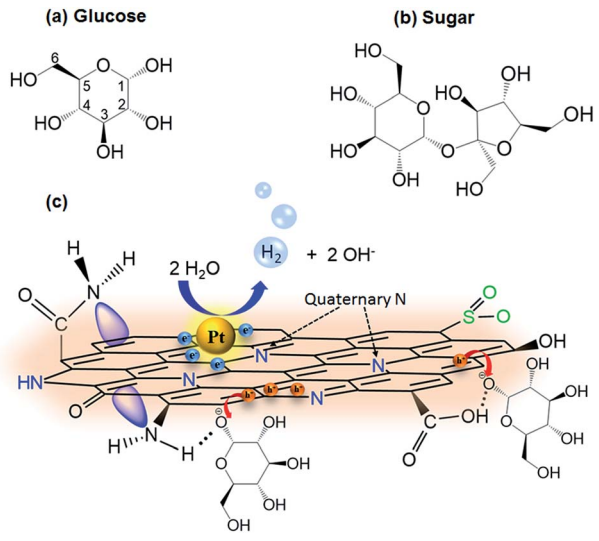

Scheme 1 (a) Structure of glucose. (b) Structure of sugar. (c) Conceptual illustration of a graphene oxide dot (GOD). The basal plane of the GODs synthesized in the present work has a high concentration of quaternary N that repairs the vacancy defects. The functional groups effectively adsorb deprotonated glucose molecules through hydrogen-bonding in a basic environment.

Graphene oxide (GO) with its tunable-structure feature can serve as a photocatalyst.[39] The oxygen functionalities on the graphene substrate enlarge the bandgap and enable GO to easily disperse in an aqueous solution. However, oxidized graphene contains vacancy defects, detrimental to the photocatalytic activity.[40] Doping heteroatoms into GO matrices repairs the defects and modulates the electronic structure to increase their photocatalytic activity.[41–45] In the present study, N and S are introduced into the GO matrix to effectively repair the vacancy defects and facilitate the separation of photogenerated charges for interfacial reactions (*i.e.*, reactions (R2) and (R3)) over the catalysts (Scheme 1c).

In this study, S and N codoped GO dots (SNGODs), synthesized by treating GO with ammonia and sulfur, exhibited high content of quaternary N (or graphitic N) that was located inside the graphene sheets (see Scheme 1c) and repaired the vacancy defects of the basal plane. The peripheral N and S functionalities of the SNGODs produced electron resonance between the graphitic-π orbital and nonbonding states (n-states) of the N and S atoms, resulting in the reduction of the bandgap and extension of the photogenerated charge lifetime. Pt-deposited SNGODs were stable in photocatalytic reforming of sugar and glucose into H_2, with apparent quantum yields (AQYs) of 11% and 7.4%, respectively, under monochromatic irradiation at 420 nm. The high quantum yields in H_2 production demonstrated the superiority of using graphene dots in the photocatalytic reforming of biomass into H_2.

2. Results and discussion

2.1. Chemical structure and morphology of photocatalysts

The SNGODs were sequentially synthesized by annealing GO in the presence of sulfur and ammonia at 600 °C, oxidizing the annealed product to dots, and finally, autoclaving the dots in ammonia solution at 140 °C. For comparison, we synthesized NGODs by replacing the sulfur and ammonia used in the GO annealing with argon. The autoclaving treatment of both SNGODs and NGODs in ammonia solution could passivate the GO dots by converting oxygen functionalities into nitrogen functionalities.[46,47] Fig. S1a and b† illustrate transmission electron microscopy (TEM) images of the NGODs and SNGODs, respectively, and the histograms in the insets indicate the size distributions of the samples; both samples have similar sizes of 2–6 nm. Fig. S1c and d† present high-resolution TEM (HRTEM) images of the NGODs and SNGODs, respectively, indicating a lattice fringe spacing of 0.213 nm corresponding to the *d*-spacing of the graphene $\{1\bar{1}00\}$ lattice planes.[48–50] The HRTEM images reveal that these graphene-based catalysts are crystalline. The annealing codoping of N and S atoms did not change the physical structure of the graphene-based particles relative to that of the particles obtained from annealing with argon.

Fig. S2a and b† illustrate the full-range X-ray photoelectron spectroscopy (XPS) spectra of the NGODs and SNGODs. In both

figures, the C 1s, N 1s, and O 1s peaks were located at binding energies of 284, 400, and 532 eV, respectively. The spectrum of the SNGODs exhibited additional S 2p and S 2s peaks at 168 and 232 eV, respectively (Fig. S2b†), confirming the presence of S in the SNGODs. Table 1 lists the atomic ratios of (O 1s)/(C 1s), (N 1s)/(C 1s), and (S 2p)/(C 1s) determined from the XPS spectra. The NGODs and SNGODs exhibited similar (O 1s)/(C 1s) ratios. The SNGODs exhibited a (N 1s)/(C 1s) ratio of 15%, which was higher than that of the NGODs (7.5%), indicating that the annealing codoping of N and S promoted the introduction of N. The annealing codoping also led to a (S 2p)/(C 1s) ratio of 6.5% for the SNGODs.

Fig. 1a and b present a comparison of the C 1s spectra of the NGODs and SNGODs. The spectra comprise peaks from deconvolution of the C–C (284.6 eV), C–N (285.8 eV), C–O (286.5 eV), C=O (288.0 eV), and O–C=O (289.0 eV) groups.[51,52] Table 1 indicates the composition of the peaks contributing to the C 1s spectra. The C–O indicated the characteristic bonding of epoxy, tertiary alcohol, and phenol groups, and the C=O and O–C=O were those of ketone and carboxylic groups, respectively.[53] The annealing codoping of N and S resulted in an increase in the C–N content at the expense of the C–O content for the SNGOD.[9] The C 1s spectrum of the SNGODs demonstrated a strong $\pi \rightarrow \pi^*$ shakeup satellite peak (290.8 eV) of sp^2-C, indicating that the annealing with sulfur and ammonia healed vacancies on graphene by replacing oxygenated sites with patching N atoms to improve the resonance intensity in the graphitic π matrix.[54]

Fig. 1c and d illustrate the focused N 1s spectra, comprising the peaks of pyridine-like (398.4 eV), amino (–NH_2, 399.2 eV), pyrrolic-like (399.1 eV), quaternary (400.7 eV), and amide (N–C=O, 401.2 eV) functionalities.[55–58] The peak areas and composition data depicted in Table 1 indicate that the annealing treatment with sulfur and ammonia increased the nitrogen content of the SNGODs through the introduction of high-binding-energy nitrogen functionalities—pyrrolic, quaternary, and amide groups. The quaternary N repaired the vacancies on the graphitic plane,[59,60] whereas the peripheral amide N donated its n-state (lone-pair) electrons to conjugate with the graphitic π system (Scheme 1c).[41] Analysis of the N 1s spectra explains the reason that the C 1s spectrum of the SNGODs exhibited a strong $\pi \rightarrow \pi^*$ shakeup satellite peak. NGODs, which were solely N-doped, exhibited low quaternary-N content and a weak $\pi \rightarrow \pi^*$ shakeup peak, indicating that sole N-doping is less effective in repairing the graphitic plane. Our auxiliary XPS study on SGODs, solely S-doped, revealed that SGODs did not exhibit any $\pi \rightarrow \pi^*$ shakeup peak (Fig. S3†), indicating that sole S-doping did not repair the graphitic plane. The comparison of the intensities of the $\pi \rightarrow \pi^*$ shakeup peak strongly supports that the S and N codoping patched the vacancy defects of the graphene framework.

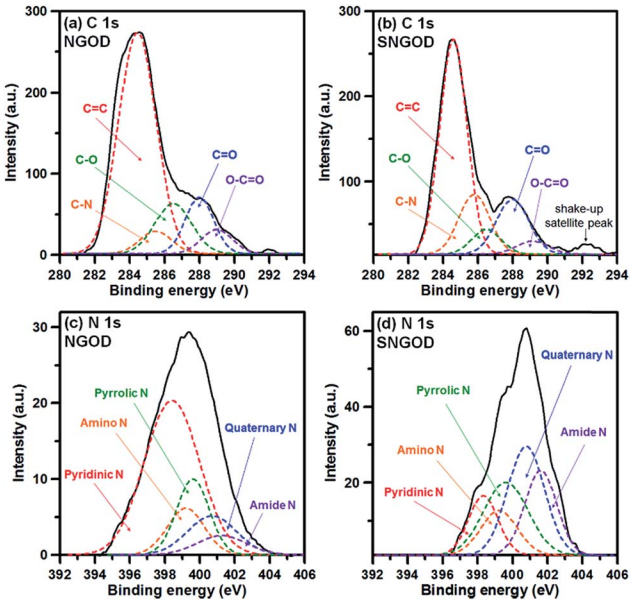

Fig. 1 XPS spectra of the photocatalysts. C 1s XPS spectra of (a) NGOD and (b) SNGOD. N 1s spectra of (c) NGOD and (d) SNGOD.

Table 1 Atomic ratios (O 1s)/(C 1s), (N 1s)/(C 1s), and (S 2p)/(C 1s) determined from the full-range XPS spectrum (Fig. S2a and b), carbon bonding compositions determined from the C 1s XPS (Fig. 1a and b), nitrogen bonding compositions determined from the N 1s XPS (Fig. 1c and d), and sulfur bonding compositions determined from the S 2p XPS (Fig. S2c) for the NGODs and SNGODs

	Atomic ratio	Carbon bonding composition (%)				
	O 1s/C 1s	C–C	C–N	C–O	C=O	O–C=O
NGOD	57%	63	5.6	14	12	5.7
SNGOD	59%	62	13	8.1	12	5.3
	Atomic ratio	Nitrogen functionality composition (% of C 1s)				
	N 1s/C 1s	Pyridine	Amino	Pyrrolic	Quaternary	Amide
NGOD	7.5%	3.8	0.8	1.2	1.1	0.6
SNGOD	15%	1.9	1.8	3.6	4.4	2.9
	Atomic ratio	Sulfur functionality composition (% of C 1s)				
	S 2p/C 1s	–SH	C–S–C	C=S	C–SO_2	C–SO_3
SNGOD	6.5%	0.2	0.3	0.6	4.6	0.8

Fig. S2c† illustrates the focused S 2p spectrum of the SNGODs. The spectrum consists of thiol (–SH, 162.3 eV), –C–S–C– (163.9 eV), –C=S– (165.1 eV), –C–SO_2– (168.3 eV), and –C–SO_3– (170.5 eV).[61–64] The –C–S–C– and –C=S– peaks were spin–orbit couples of thiophene S.[62,65,66] The peaks with high binding energies were contributed by oxidized S atoms, located at the edges and vacancy defects of graphene.[51,62,67] These oxidized S atoms were the dominant S species of the SNGODs. Oxidized S would be positively charged because of the high electronegativity of the neighboring O atoms and would therefore be attractive to photogenerated holes during a photocatalytic reaction.

Fig. 2 presents the Raman spectra of the NGODs and SNGODs. Both spectra exhibited D (1370 cm^{-1}) and G (1600 cm^{-1}) bands corresponding to sp^3-associated carbon and the vibration of the sp^2-bonded graphitic carbon, respectively,

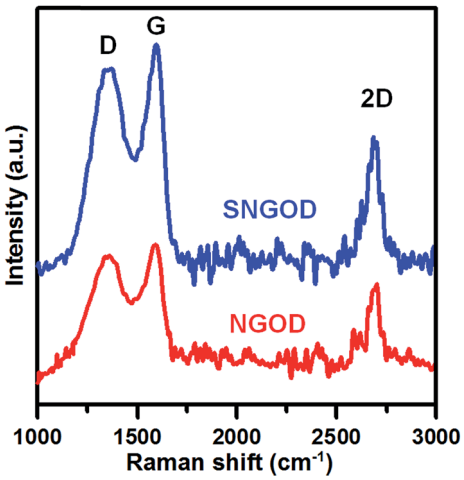

Fig. 2 Raman spectra of the NGOD and SNGOD.

in a two-dimensional hexagonal lattice.[68–71] The appearance of the double-resonance 2D band at 2710 cm^{-1} indicated that graphene dots comprised fewer than three layers of stacked graphene.[59] The SNGODs exhibited a lower D-to-G peak intensity ratio (0.79) than did the NGODs (0.95), reflecting that the comprehensively introduced quaternary N repaired the vacancy defects in the SNGODs and induced a strong G band.[44,68] Furthermore, the SNGODs exhibited a sharp 2D band, confirming that the annealing treatment with sulfur and ammonia produced intact graphitic domains in the SNGODs.

Fig. S4a† presents the Fourier transform infrared (FTIR) spectra of the NGODs and SNGODs. The spectra exhibit characteristic bands around 870 cm^{-1} for $-NH_2$ wagging vibrations, 1110 cm^{-1} for amino C–N stretching vibrations, 1230 cm^{-1} for aromatic C–N stretching in the amino groups, 1386 cm^{-1} for C–N stretching in the amide groups, 1430 cm^{-1} for benzenoid (*i.e.*, amino form) C=C stretching, 1610 cm^{-1} for quinonoid (*i.e.*, imino form) C=C stretching, 1730 cm^{-1} for HO–C=O or C=O stretching, 2800–3100 cm^{-1} for C–H vibrations,[72–74] and 3000–3300 cm^{-1} for N–H vibrations in the amino or amide groups.[67] A band at approximately 650 cm^{-1} of the SNGOD spectrum corresponded to C–S stretching.[75–77] The FTIR analysis reflected that the annealing treatment with sulfur and ammonia for the SNGODs increased the content of C–N and N–H bonds, which agreed with the findings of the XPS analysis. The high intensity of the benzenoid and quinonoid C=C stretching in the SNGODs indicated a strong donation of electrons from the nitrogen functionalities to the graphitic π system.

2.2. Optical and electronic properties of photocatalysts

Fig. 3a depicts the optical absorption spectra of the NGOD and SNGOD aqueous suspensions (the concentrations were approximately 0.18 g L^{-1}). Both suspensions exhibited broad absorption in the UV and visible light regions. The suspension photographs (the inset of Fig. 3a) indicate that the color of the SNGOD suspension was darker than that of the NGOD, indicating that the annealing treatment with sulfur and ammonia enhanced the light absorbance in the visible light region. The

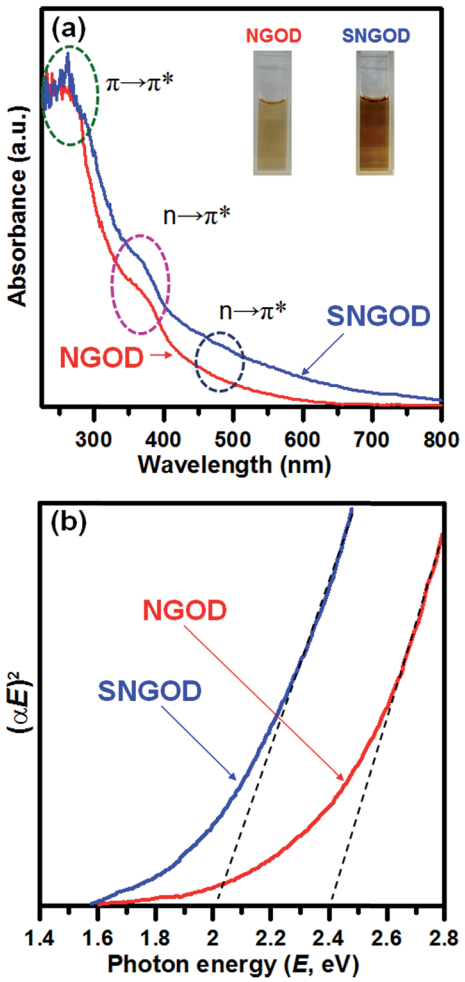

Fig. 3 (a) Optical absorption spectra of the NGOD and SNGOD aqueous suspensions, with the inset showing the photographs of the suspensions under daylight. (b) Plots of $(\alpha E)^2$ against photon energy (E) for the NGOD and SNGOD suspensions (α is the absorbance).

spectra of both suspensions exhibited a strong absorption band at approximately 230–265 nm (5.4–4.7 eV), corresponding to the energy required for the π → π* transition in the sp^2 domain of graphene-based materials.[75,78–80] An absorption shoulder appears at 335–400 nm in the spectra of both SNGODs and NGODs, indicating an n → π* transition from the n-states (*i.e.*, the heteroatom nonbonding electron states conjugated with the graphitic-π orbital) to the π* orbital.[81–84] The absorption in the visible light region (>400 nm) may have corresponded to an n → π* transition from the n-states conjugated with the π orbital of C=N and C=S double bonds to the π*.[85] The n-state electrons of the S and N atoms on the graphene dots extended the π conjugated system and enabled long-wavelength visible light absorption for the SNGODs (Fig. 3a). Extended light absorption is beneficial for the photocatalytic H_2 evolution reaction under solar illumination.

The direct bandgap energies of the NGODs and SNGODs were determined from the absorption data by plotting the square of the absorption energy (αE, where α is the absorbance and E the photon energy) against E. Fig. 3b illustrates that the

bandgap energies of the NGODs and SNGODs were determined to be 2.4 and 2.0 eV, respectively, through linear extrapolation to the abscissa. In the SNGODs, the n-state electrons of the N and S atoms strongly conjugated with the π electrons in the N- and S-doped graphitic domains, upshifting the top-of-valence band (tVB) and narrowing the bandgap.

Fig. S5a† shows the PL spectra of the NGOD and SNGOD aqueous suspensions under an excitation illumination of 405 nm in wavelength. Both samples emitting light show peaks at approximately 540 nm. The SNGODs exhibited stronger PL emission than the NGODs, indicating that the S and N codoping has repaired the vacancy defects and passivated the surface for effective PL emission. Fig. S5b† presents the time-resolved PL decay for the samples under 405 nm excitation. We simulated the decay curves by using the bi-exponential intensity function $I(t) = A_1e^{-t/\tau_1} + A_2e^{-t/\tau_2}$, where A_1 (or A_2) and τ_1 (or τ_2) are the percentage contribution and value of the shorter (or longer) lifetime component, respectively. The average lifetime (τ_{ave}) was obtained according to $\tau_{ave} = (A_1\tau_1^2 + A_2\tau_2^2)/(A_1\tau_1 + A_2\tau_2)$. The simulation parameters are listed in Table S1,† showing that the τ_{ave} values of the SNGODs and NGODs were 5.2 and 6.9 ns, respectively. The patched surface of the SNGODs resulted in a prolonged charge lifetime, which would be advantageous to the charge transfer required in the reforming reaction.

The photocatalytic redox reactions were closely related to the tVB and the bottom-of-conduction band (bCB) levels of the catalysts. In this study, we used ultraviolet photoelectron spectroscopy (UPS) to determine the tVB levels. The tVB levels of the NGODs and SNGODs were −6.3 and −5.8 eV (*vs.* vacuum), respectively, which were calculated by subtracting the width of the UPS spectra (Fig. S6†) from the excitation energy (21.2 eV). The difference in the tVB levels reflected that S and N codoping promoted orbital conjugation. The tVB level increased by 0.5 eV as a result of the π orbital interaction with the introduced n-states of the S and N atoms.[41,85] By incorporating the bandgap energy and tVB data, we created a schematic (Fig. 4) illustrating the band energy levels of the NGODs and SNGODs relative to the energy levels of H_2 and O_2 generated from the water splitting reactions. The bCB levels of the NGODs and SNGODs (−3.9 and −3.8 eV *vs.* vacuum, respectively) were similar and high enough to produce H_2. The smaller bandgap of the SNGODs was primarily attributable to the tVB upshift, resulting from the conjugation of the π orbital with the n-states of the doped S and N atoms.

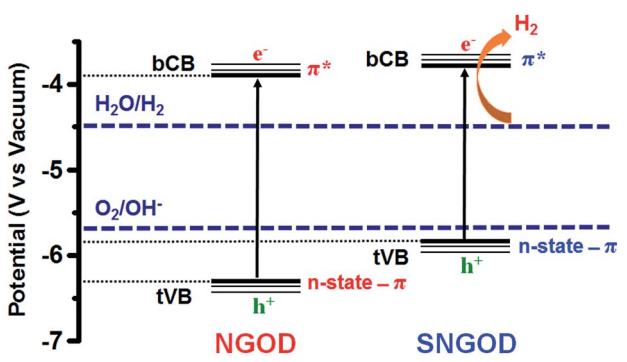

Fig. 4 Schematic energy-level diagrams of the NGODs and SNGODs relative to the levels of H_2 and O_2 generation from water. The tVB (top-of-valence band) levels are the n-state conjugated π orbitals and bCB (bottom-of-conduction band) levels are the π* orbitals.

Previous studies reported that the intermediate radical species of (R4), *i.e.*, RHCO•, injected electrons into the CB of a semiconductor in glucose photoreforming according to:[32,35]

$$RHCO^{\bullet} \rightarrow RC{=}O + H^+ + e^-. \quad (R5)$$

If (R5) contributed to (R1), only one photo-electron was needed to produce one H_2 molecule. However, the bCB levels of the NGOD and SNGOD catalysts are higher than the redox level of (R5) (*i.e.*, −4.2 eV *vs.* vacuum).[86] We therefore ruled out the possibility of injection of (R5)-derived electrons into the CB of our catalysts for H_2 evolution. The high bCB levels of our catalysts resulted in large overpotentials for the HER, explaining the high photocatalytic reforming activity that will be presented in the following discussion.

2.3. Photocatalytic reforming of sugar and glucose into H_2

To analyze the photocatalytic ability of the NGODs and SNGODs to reform sugar and glucose into H_2 in aqueous solutions, we used a gas-enclosed system with externally visible light irradiation (420 nm < λ < 800 nm) at an intensity of 35 mW cm^{-2}. Before conducting the reforming reaction, the catalysts were loaded with 5 wt% Pt as a cocatalyst through *in situ* photodeposition. The catalysts exhibited the maximal activity for H_2 production at a solution pH value of 10 (Fig. S7†). The effect of the solution pH on the H_2 production involves the chemical-state variation of sugar and glucose and the redox potential change of H_2 evolution.[3] In a basic environment, sugar and glucose molecules are deprotonated and become anions, which are more efficient at capturing holes than the molecules.[16,37] However, increasing the solution pH value also upshifts the redox potential of H_2 evolution, resulting in a decrease in the overpotential for H_2 production.[21,87] The optimal pH value for the present system was 10.

Fig. 5 presents the time course of H_2 production from sugar and glucose in aqueous solutions (0.35 mol L^{-1}) over 0.4 g of the catalysts at a pH of 10. In both sugar and glucose reforming reactions, the SNGODs exhibited higher photocatalytic activity (corresponding to 221 and 164 μmol h^{-1} g^{-1} of H_2 production from sugar and glucose, respectively) than the NGODs; the H_2 production rate for the SNGODs was approximately three times that of the NGODs. The intact graphitic domains and strong conjugation between graphitic-π orbitals and nitrogen n-states in the SNGODs potentially facilitated the separation of photogenerated charges (Scheme 1c) and therefore enhanced the photocatalytic activity.[88] The H_2 production rate was higher for sugar reforming than for glucose reforming. Moreover, the water solubility of sugar is higher than that of glucose, and thus, a superior molecular dispersion; this may be the reason for the higher H_2 production rate of sugar reforming.

Fig. S8† presents the time course of H_2 evolution from the sugar aqueous solution containing bare SNGODs. The rate of H_2 production over the bare SNGODs was much lower than that

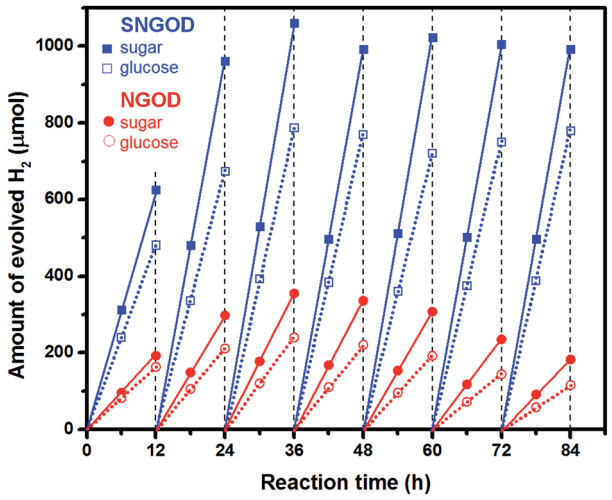

Fig. 5 The time course of H_2 production from sugar and glucose (0.35 mol L^{-1}) aqueous solutions (at a pH of 10) containing 5 wt% Pt deposited SNGODs and NGODs (0.4 g), with several interventions for evacuating the system. The system was irradiated by visible light (420 nm < λ < 800 nm) at an intensity of 35 mW cm^{-2}.

over the Pt-deposited SNGODs (Fig. 5), indicating the necessity of the Pt cocatalyst in the H_2 evolution reaction. However, our auxiliary experiment shows that the Pt cocatalyst alone produced only a negligible amount of H_2 because of the lack of light-absorbing agents such as SNGODs.

For the purpose of comparison, we evaluated the activity of TiO_2, the most-used catalyst in this reforming, in our photocatalytic reforming system. Fig. S9† shows H_2 evolution from sugar and glucose aqueous solutions containing Pt-deposited TiO_2 (P25, Degussa) over a period of 36 h. The photocatalytic reaction system was identical to that used for testing the Pt-deposited SNGODs and NGODs. The rates of H_2 production over the Pt-deposited TiO_2 were much lower than those over the Pt-deposited SNGODs (Fig. 5). This comparison demonstrates the superiority of the functionalized graphene dots in photocatalytic reforming for H_2 production.

To examine the chemical stability of the photocatalysts in the reaction, we conducted FTIR analysis on the NGODs and SNGODs after a photocatalytic reaction. Fig. S4b† shows the FTIR spectra of the NGODs and SNGODs after a 60 h photocatalytic reaction. Compared to the spectra of the samples before the reaction (Fig. S4a†), the spectra of the samples after the reaction exhibited a minor reduction in the absorption peak intensities. This comparison indicates the high stability of the functionalized graphene dots as photocatalysts in the photocatalytic reforming reaction.

In this study, we evaluated the AQY for H_2 production under monochromatic irradiation at 420 nm to quantitatively illustrate the activity of these graphene-based photocatalysts. The AQY of H_2 production was calculated using the following equation:

$$\mathrm{AQY} = \frac{\text{number of evolved } H_2 \text{ molecules} \times 2}{\text{number of incident photons}} \times 100\%,$$

where the calculated incident photon flux was 93.28 μmol h^{-1}. We used (R1) to evaluate the AQY for H_2 production, eliminating the contribution from (R5). Fig. 6a depicts the rates of H_2 production from aqueous sugar and glucose solutions containing the NGOD and SNGOD catalysts. The AQYs for the sugar and glucose solutions were, respectively, 11% and 7.4% over the SNGODs and 3.2% and 2.4% over the NGODs. The manipulation of the electronic structure (with S and N codoping) for charge generation and separation and the high affinity for sugar and glucose enabled the SNGODs to effectively reform sugar and glucose under illumination.

Fig. 7 presents the electron paramagnetic resonance (EPR) spectra of the sugar-reforming solutions with 365 nm irradiation for 30 min (red profiles). Compared with the irradiated solutions, the nonirradiated solutions exhibited negligible peaking signals (black profiles). The irradiated NGOD-containing solution exhibited Lorentzian lines centered at a g value of 2.00226 (Fig. 7a), which signaled the presence of free electrons on the π-conjugated GO plane.[89] The signal indicated

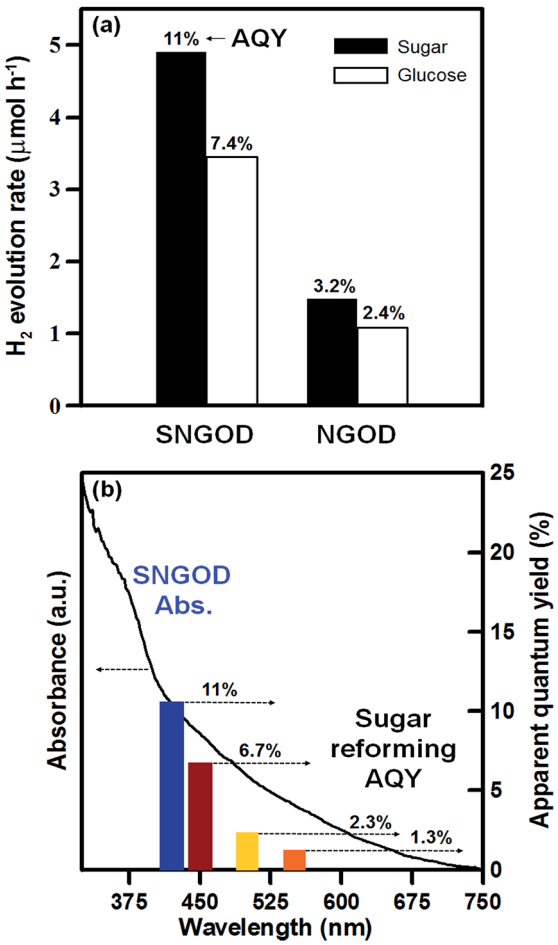

Fig. 6 (a) The rates of H_2 production from aqueous sugar and glucose solutions containing the Pt-deposited NGOD and SNGOD catalysts under 420 nm monochromatic light irradiation. (b) Absorption spectrum of the aqueous SNGOD suspension and the apparent quantum yields for the Pt-deposited SNGODs under 420, 450, 500, and 550 nm monochromatic light irradiations, of which the illumination intensities were 0.588, 0.798, 0.926, and 0.934 mW cm^{-2}, respectively.

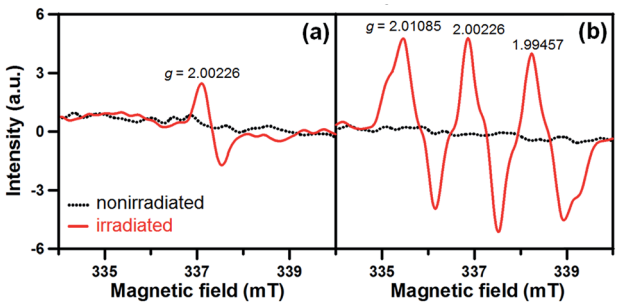

Fig. 7 Electron paramagnetic resonance spectra of the sugar-reforming solutions containing the (a) NGOD catalyst and (b) SNGOD catalyst. The results with 365 nm irradiation for 30 min (red profiles) and without any irradiation (black profiles) are presented.

that the adsorbed sugar anions or molecules attracted holes in the NGODs to induce the separation of photogenerated charges. Fig. 7b illustrates that the irradiated SNGOD-containing solution exhibited a signal stronger than that of the NGOD-containing solution. Moreover, the SNGOD signal exhibited a hyperfine splitting feature that resulted from the interaction of electron spins with nearby magnetic nuclei.[90] A magnetic nucleus with a quantum number (I) would split a single EPR line into $2I + 1$ lines; for example, ^{14}N ($I = 1$) would lead to triple splitting.[91] The SNGODs exhibited a three-line EPR signal at g values of 2.01085, 2.00226, and 1.99457. The high quaternary N content of the SNGOD catalyst indicates the coupling of the N atoms (as the magnetic nuclei) with electrons delocalized over aromatic rings, thereby inducing such hyperfine (triple) splitting as shown in Fig. 7b. The accompanied high EPR intensity (*i.e.*, high free electron concentration) of the SNGODs confirms that the high content of quaternary N patched the GO sheets to promote electron delocalization.

Fig. 6b presents the incident wavelength dependence of the photocatalytic activity of the SNGODs in sugar reforming. The AQY decreased with increasing incident wavelengths according to the trend of light absorbance variation. However, the decrease in the AQY was more severe than that in light absorbance. Long-wavelength illumination may have resulted in a low probability of charge excitation to the bCB and therefore a low AQY. Nevertheless, an AQY of 1.3% was achieved at a long wavelength of 550 nm. The outstanding performance of the SNGODs demonstrated a means for photocatalytically reforming biomass into H_2 by using environment friendly carbon-based catalysts.

3. Conclusions

This study demonstrated the feasibility of using graphene-based media for photocatalysts to reform sugar and glucose under visible light irradiation. The electronic structure of graphene-based media can be easily tuned by doping heteroatoms into the graphitic framework. The semiconductor GO was codoped with S and N and doped with only N and further oxidized for size reduction to form SNGOD and NGOD photocatalysts, respectively. S and N codoping created quaternary N, which repaired the vacancy defects of the graphitic plane and introduced periphery amide groups, in which the nitrogen n-states donated electrons to the graphitic-π orbital to improve orbital conjugation. The enlarged domain for electron resonance in the SNGODs reduced the bandgap and induced delocalization of photogenerated charges. SNGOD activity was three times that of the NGODs in the photocatalytic reforming of sugar and glucose. The EPR analysis confirmed that the quaternary N induced electron delocalization and thus charge separation in the SNGODs, thus enhancing their reforming activity. The SNGOD-photocatalyzed reforming of sugar and glucose produced H_2 AQYs of 11% and 7.4%, respectively, under monochromatic irradiation of 420 nm. Our work demonstrated the feasibility of using carbon-based materials, which can be grafted with functional groups to attract biomass molecules, as the media for photocatalytically reforming biomass into H_2. Use of environmentally benign carbon-based photocatalysts for biomass reformation can be implemented to achieve a sustainable reforming method for hydrogen energy production.

4. Experimental section

4.1. Photocatalyst synthesis

GO was prepared using a natural graphite powder (Bay carbon, SP-1, USA) according to a modified Hummers' method.[92] The graphite powder (5 g) and $NaNO_3$ (2.5 g; ≥99.0%, Merck, Germany) were added to a concentrated H_2SO_4 solution (18 M, 150 mL; Wako, Japan) in an ice bath. $KMnO_4$ (15 g; ≥99.0%, J.T. Baker, USA) was gradually added with stirring. The mixture was stirred at 35 °C for 4 h to allow oxidation, and thereafter deionized water (230 mL) was slowly added to the mixture and stirred at 98 °C for 15 min. The mixture was further diluted to 700 mL and stirred for 30 min. The reaction was terminated by adding H_2O_2 (10 mL, 30 wt%; Shimakyu, Japan) while stirring at room temperature. Multiple washings were conducted with deionized water (4 × 500 mL), and the precipitate of the final slurry was freeze-dried for 24 h to obtain the GO specimens.

Nitrogen and sulfur codoped graphene (SNG) was synthesized by treating the mixture of the as-prepared GO and S powder (99.999%, Acros, USA) in a flow of NH_3 gas at 600 °C for 3 h. The SNG (0.2 g) sample was oxidized in concentrated HNO_3 (60 mL, 60%; Showa, Japan) at room temperature for 12 h. The solution was subsequently treated ultrasonically for 12 h, which was followed by heating to 140 °C in an oven with evacuation to remove the residual HNO_3. The product was dispersed in deionized water and centrifuged to remove the precipitate and achieve a dot suspension.

SNGODs were synthesized by treating 0.4 g of the dots with 100 mL of ammonia solution (30 wt% in water; Sigma-Aldrich, USA) in an autoclave at 140 °C for 5 h. After the autoclaving process, the solution was heated to 100 °C in an oven to remove the residual ammonia solution and it was then dispersed in deionized water. NGODs were also synthesized in the same manner, except that the S and NH_3 treatment at 600 °C was replaced by Ar treatment. SGODs were also synthesized in the same manner as that for SNGODs except that the NH_3 flow was

replaced by an Ar flow for the 600 °C-treatment and the 140 °C-autoclaving in the ammonia solution was omitted.

4.2. Photocatalyst characterization

XPS (AXIS Ultra DLD, Kratos, UK) with Al Kα radiation was used to quantitatively analyze the chemical composition of the catalysts. The C 1s, N 1s, and S 2p spectra were decomposed into constituent peaks using a Gaussian fitting function. A TEM (Jeol 2100F, Japan) was used to determine the microstructure of the samples. Raman spectra were recorded using a DXR Raman microscope (Thermo Fisher Scientific Inc., USA) at room temperature and under a laser with an excitation wavelength of 532 nm. FTIR spectra were recorded using a Nicolet 6700 spectrometer (Thermo Fisher Scientific Inc., USA) at room temperature. The optical absorption spectrum of the catalysts in water suspensions (all at 0.18 mg mL^{-1}) was obtained by placing the solution in a 1 cm quartz cuvette for analysis using a Hitachi U-4100 (Japan) spectrophotometer. UPS (Sigma Probe, Thermo VG Scientific, UK) with He I excitation (21.2 eV) was performed to determine the valence band edges. EPR spectra were recorded on a Magnettech model MS5000 spectrometer (Germany) using a 4 W mercury lamp (UVP Instrument, USA) for the light source. The PL spectra of the NGODs and SNGODs in aqueous solution (0.18 mg mL^{-1}) were measured at ambient temperature using a fluorescence spectrophotometer (F-700, Hitachi, Japan). For PL lifetime determination, the PL spectroscopy measurements were recorded using a spectrofluorometer (FS5, Edinburgh Instruments, UK) under 405 nm excitation. Nonlinear least square algorithms were used to fit the PL lifetime decay curves.

4.3. Photocatalytic activity measurement

Photocatalytic reactions were conducted at approximately 25 °C in a gas-enclosed side irradiation system. The NGOD or SNGOD catalysts (0.4 g) were suspended in 250 mL of 0.35 mol L^{-1} sugar (sucrose; ≥99.5%, J.T. Baker, USA) or glucose (D-(+)-glucose; ≥99.5%, J.T. Baker, USA) aqueous solution in a Pyrex vessel. The pH value was adjusted using HCl and NaOH solutions. The solution contained $H_2PtCl_6 \cdot 6H_2O$ (16 mg, 99.9%; Alfa Aesar, USA) for *in situ* deposition of 5 wt% Pt on the catalysts. The photocatalytic reactions were initiated with side illumination from a 300 W xenon lamp (Oriel Instruments, model 66901, USA), which had an incident intensity of 35 mW cm^{-2}. The wavelength was limited to 420–800 nm using a UV cut-off filter (Asahi Spectra, XUL0422, USA) and an IR-cutoff filter (Asahi Spectra, XIS0810, USA). For quantum yield measurements, we used 420, 450, 500, and 550 nm band-pass filters (Newport, 20BPF10-420, USA) to obtain monochromatic irradiation. The intensity of the light irradiated on the reacting system was determined using a photodetector (Oriel Instrument, model 71964, USA). The quantity of H_2 produced was determined using gas chromatography (Hewlett-Packard 7890, USA; molecular sieve 5A column, thermal conductivity detector, argon carrier gas).

Conflicts of interest

There are no conflicts to declare.

Acknowledgements

This work was financially supported by the Ministry of Science and Technology in Taiwan through grant numbers 107-2221-E-006-110-MY3, 107-2221-E-006-111-MY3, 107-2622-8-006-015, and 107-3113-E-006-006, Hierarchical Green-Energy Materials (Hi-GEM) Research Center and Center of Applied Nanomedicine at National Cheng Kung University from The Featured Areas Research Center Program within the framework of the Higher Education Sprout Project by the Ministry of Education (MOE) and Ministry of Science and Technology (MOST 107-3017-E-006-003) in Taiwan.

Notes and references

1 P. Chowdhury, G. Malekshoar and A. K. Ray, *Inorganics*, 2017, **5**, 34.
2 S. S. K. Ma, T. Hisatomi and K. Domen, *J. Jpn. Pet. Inst.*, 2013, **56**, 280–287.
3 X. Fu, J. Long, X. Wang, D. Y. Leung, Z. Ding, L. Wu, Z. Zhang, Z. Li and X. Fu, *Int. J. Hydrogen Energy*, 2008, **33**, 6484–6491.
4 C. H. Liao, C. W. Huang and J. Wu, *Catalysts*, 2012, **2**, 490–516.
5 Z. Sun, H. Zheng, J. Li and P. Du, *Energy Environ. Sci.*, 2015, **8**, 2668–2676.
6 A. S. Hainer, J. S. Hodgins, V. Sandre, M. Vallieres, A. E. Lanterna and J. C. Scaiano, *ACS Energy Lett.*, 2018, **3**, 542–545.
7 T. Jafari, E. Moharreri, A. S. Amin, R. Miao, W. Song and S. L. Suib, *Molecules*, 2016, **21**, 900.
8 E. A. Kozlova and A. V. Vorontsov, *Int. J. Hydrogen Energy*, 2010, **35**, 7337–7343.
9 L. C. Chen, C. Y. Teng, C. Y. Lin, H. Y. Chang, S. J. Chen and H. Teng, *Adv. Energy Mater.*, 2016, **6**, 1600719.
10 C. J. Chang, Y. G. Lin, H. T. Weng and Y. H. Wei, *Appl. Surf. Sci.*, 2018, **451**, 198–206.
11 D. Xu, L. Li, R. He, L. Qi, L. Zhang and B. Cheng, *Appl. Surf. Sci.*, 2018, **434**, 620–625.
12 Z. Wang, J. Hou, C. Yang, S. Jiao, K. Huang and H. Zhu, *Energy Environ. Sci.*, 2013, **6**, 2134–2144.
13 L. Yang, D. Zhong, J. Zhang, Z. Yan, S. Ge, P. Du, J. Jiang, D. Sun, X. Wu and Z. Fan, *ACS Nano*, 2014, **8**, 6979–6985.
14 S. W. Cao, Y. P. Yuan, J. Fang, M. M. Shahjamali, F. Y. Boey, J. Barber, S. C. J. Loo and C. Xue, *Int. J. Hydrogen Energy*, 2013, **38**, 1258–1266.
15 T. Kawai and T. Sakata, *Nature*, 1980, **286**, 474.
16 M. Ilie, B. Cojocaru, V. I. Parvulescu and H. Garcia, *Int. J. Hydrogen Energy*, 2011, **36**, 15509–15518.
17 G. Wu, T. Chen, G. Zhou, X. Zong and C. Li, *Sci. China, Ser. B: Chem.*, 2008, **51**, 97–100.

18 J. C. Colmenares, A. Magdziarz, M. A. Aramendia, A. Marinas, J. M. Marinas, F. J. Urbano and J. A. Navio, *Catal. Commun.*, 2011, **16**, 1–6.
19 S. Q. Peng, Y. J. Peng, Y. X. Li, G. X. lu and S. B. Li, *Res. Chem. Intermed.*, 2009, **35**, 739–749.
20 Y. Li, J. Wang, S. Peng, G. Lu and S. Li, *Int. J. Hydrogen Energy*, 2010, **35**, 7116–7126.
21 D. Jing, M. Liu, J. Shi, W. Tang and L. Guo, *Catal. Commun.*, 2010, **12**, 264–267.
22 P. Gomathisankar, D. Yamamoto, H. Katsumata, T. Suzuki and S. Kaneco, *Int. J. Hydrogen Energy*, 2013, **38**, 5517–5524.
23 M. R. St. John, A. J. Furgala and A. F. Sammells, *J. Phys. Chem.*, 1983, **87**, 801–805.
24 X. Fu, X. Wang, D. Y. C. Leung, W. Xue, Z. Ding, H. Huang and X. Fu, *Catal. Commun.*, 2010, **12**, 184–187.
25 V. Vaiano, G. Iervolino, G. Sarno, D. Sannino, L. Rizzo, J. J. Murcia Mesa, M. C. Hidalgo and J. A. Navío, *Oil Gas Sci. Technol*, 2015, **70**, 891–902.
26 C. Li, H. Wang, J. Ming, M. Liu and P. Fang, *Int. J. Hydrogen Energy*, 2017, **42**, 16968–16978.
27 A. Kudo and Y. Miseki, *Chem. Soc. Rev.*, 2009, **38**, 253–278.
28 D. W. Wakerley, M. F. Kuehnel, K. L. Orchard, K. H. Ly, T. E. Rosser and E. Reisner, *Nat. Energy*, 2017, **2**, 17021.
29 A. N. Zulkifili, A. Fujiki and S. Kimijima, *Appl. Sci.*, 2018, **8**, 216.
30 M. Zhou, Y. Li, S. Peng, G. Lu and S. Li, *Catal. Commun.*, 2012, **18**, 21–25.
31 G. Iervolino, V. Vaiano, D. Sannino, L. Rizzo and P. Ciambelli, *Int. J. Hydrogen Energy*, 2016, **41**, 959–966.
32 K. E. Sanwald, T. F. Berto, W. Eisenreich, A. Jentys, O. Y. Gutiérrez and J. A. Lercher, *ACS Catal.*, 2017, **7**, 3236–3244.
33 Y. Li, D. Gao, S. Peng, G. Lu and S. Li, *Int. J. Hydrogen Energy*, 2011, **36**, 4291–4297.
34 K. C. Christoforidis and P. Fornasiero, *ChemCatChem*, 2017, **9**, 1523–1544.
35 K. E. Sanwald, T. F. Berto, W. Eisenreich, O. Y. Gutiérrez and J. A. Lercher, *J. Catal.*, 2016, **344**, 806–816.
36 I. A. Shkrob, M. C. Sauer and D. Gosztola, *J. Phys. Chem. B*, 2004, **108**, 12512–12517.
37 M. H. Du, J. Feng and S. Zhang, *Phys. Rev. Lett.*, 2007, **98**, 066102.
38 I. A. Shkrob, T. W. Marin, S. D. Chemerisov and M. D. Sevilla, *J. Phys. Chem. C*, 2011, **115**, 4642–4648.
39 T. F. Yeh, J. Cihlář, C. Y. Chang, C. Cheng and H. Teng, *Mater. Today*, 2013, **16**, 78–84.
40 J. A. Yan, L. Xian and M. Chou, *Phys. Rev. Lett.*, 2009, **103**, 086802.
41 S. H. Jin, D. H. Kim, G. H. Jun, S. H. Hong and S. Jeon, *ACS Nano*, 2013, **7**, 1239–1245.
42 Y. Zheng, Y. Jiao, L. Ge, M. Jaroniec and S. Z. Qiao, *Angew. Chem.*, 2013, **125**, 3192–3198.
43 Q. Feng, Q. Cao, M. Li, F. Liu, N. Tang and Y. Du, *Appl. Phys. Lett.*, 2013, **102**, 013111.
44 Z. Yang, Z. Yao, G. Li, G. Fang, H. Nie, Z. Liu, X. Zhou, X. a. Chen and S. Huang, *ACS Nano*, 2011, **6**, 205–211.
45 X. Li, R. Shen, S. Ma, X. Chen and J. Xie, *Appl. Surf. Sci.*, 2018, **430**, 53–107.
46 G. S. Kumar, R. Roy, D. Sen, U. K. Ghorai, R. Thapa, N. Mazumder, S. Saha and K. K. Chattopadhyay, *Nanoscale*, 2014, **6**, 3384–3391.
47 C. Zhang, R. Hao, H. Liao and Y. Hou, *Nano Energy*, 2013, **2**, 88–97.
48 S. Stankovich, D. A. Dikin, G. H. Dommett, K. M. Kohlhaas, E. J. Zimney, E. A. Stach, R. D. Piner, S. T. Nguyen and R. S. Ruoff, *Nature*, 2006, **442**, 282.
49 S. Park, J. An, R. D. Piner, I. Jung, D. Yang, A. Velamakanni, S. T. Nguyen and R. S. Ruoff, *Chem. Mater.*, 2008, **20**, 6592–6594.
50 D. C. Elias, R. R. Nair, T. Mohiuddin, S. Morozov, P. Blake, M. Halsall, A. Ferrari, D. Boukhvalov, M. Katsnelson and A. Geim, *Science*, 2009, **323**, 610–613.
51 S. Stankovich, D. A. Dikin, R. D. Piner, K. A. Kohlhaas, A. Kleinhammes, Y. Jia, Y. Wu, S. T. Nguyen and R. S. Ruoff, *Carbon*, 2007, **45**, 1558–1565.
52 H. He and C. Gao, *Chem. Mater.*, 2010, **22**, 5054–5064.
53 M. Seredych, A. V. Tamashausky and T. J. Bandosz, *Adv. Funct. Mater.*, 2010, **20**, 1670–1679.
54 R. Rozada, J. I. Paredes, S. Villar-Rodil, A. Martínez-Alonso and J. M. Tascón, *Nano Res.*, 2013, **6**, 216–233.
55 T. F. Yeh, C. Y. Teng, S. J. Chen and H. Teng, *Adv. Mater.*, 2014, **26**, 3297–3303.
56 S. Kelemen, M. Afeworki, M. Gorbaty, P. Kwiatek, M. Solum, J. Hu and R. Pugmire, *Energy Fuels*, 2002, **16**, 1507–1515.
57 R. Pietrzak, *Fuel*, 2009, **88**, 1871–1877.
58 H. Wang, T. Maiyalagan and X. Wang, *ACS Catal.*, 2012, **2**, 781–794.
59 B. Guo, Q. Liu, E. Chen, H. Zhu, L. Fang and J. R. Gong, *Nano Lett.*, 2010, **10**, 4975–4980.
60 T. F. Yeh, S. J. Chen and H. Teng, *Nano Energy*, 2015, **12**, 476–485.
61 M. Favaro, F. Carraro, M. Cattelan, L. Colazzo, C. Durante, M. Sambi, A. Gennaro, S. Agnoli and G. Granozzi, *J. Mater. Chem. A*, 2015, **3**, 14334–14347.
62 S. Yang, L. Zhi, K. Tang, X. Feng, J. Maier and K. Müllen, *Adv. Funct. Mater.*, 2012, **22**, 3634–3640.
63 Y. Su, Y. Zhang, X. Zhuang, S. Li, D. Wu, F. Zhang and X. Feng, *Carbon*, 2013, **62**, 296–301.
64 Y. Ito, W. Cong, T. Fujita, Z. Tang and M. Chen, *Angew. Chem., Int. Ed.*, 2015, **54**, 2131–2136.
65 F. Buckel, F. Effenberger, C. Yan, A. Gölzhäuser and M. Grunze, *Adv. Mater.*, 2000, **12**, 901–905.
66 I. Herrmann, U. Kramm, J. Radnik, S. Fiechter and P. Bogdanoff, *J. Electrochem. Soc.*, 2009, **156**, B1283–B1292.
67 Z. Q. Zhao, P. W. Xiao, L. Zhao, Y. Liu and B. H. Han, *RSC Adv.*, 2015, **5**, 73980–73988.
68 L. Malard, M. Pimenta, G. Dresselhaus and M. Dresselhaus, *Phys. Rep.*, 2009, **473**, 51–87.
69 H. Tetsuka, R. Asahi, A. Nagoya, K. Okamoto, I. Tajima, R. Ohta and A. Okamoto, *Adv. Mater.*, 2012, **24**, 5333–5338.
70 Y. Wang, J. Yu, W. Xiao and Q. Li, *J. Mater. Chem. A*, 2014, **2**, 3847–3855.

71 G. Zhou, L. Shen, Z. Xing, X. Kou, S. Duan, L. Fan, H. Meng, Q. Xu, X. Zhang and L. Li, *J. Colloid Interface Sci.*, 2017, **505**, 1031–1038.
72 M. Li, S. K. Cushing, X. Zhou, S. Guo and N. Wu, *J. Mater. Chem.*, 2012, **22**, 23374–23379.
73 D. Sun, R. Ban, P. H. Zhang, G. H. Wu, J. R. Zhang and J. J. Zhu, *Carbon*, 2013, **64**, 424–434.
74 J. Ryu, E. Lee, S. Lee and J. Jang, *Chem. Commun.*, 2014, **50**, 15616–15618.
75 D. Qu, M. Zheng, P. Du, Y. Zhou, L. Zhang, D. Li, H. Tan, Z. Zhao, Z. Xie and Z. Sun, *Nanoscale*, 2013, **5**, 12272–12277.
76 B. X. Zhang, H. Gao and X. L. Li, *New J. Chem.*, 2014, **38**, 4615–4621.
77 T. K. Wu, J. Gliniak, J. H. Lin, Y. T. Chen, C. R. Li, E. Jokar, C. H. Chang, C. S. Peng, J. N. Lin and W. H. Lien, *ChemSusChem*, 2017, **10**, 3260–3267.
78 Z. Luo, Y. Lu, L. A. Somers and A. C. Johnson, *J. Am. Chem. Soc.*, 2009, **131**, 898–899.
79 G. Eda, Y. Y. Lin, C. Mattevi, H. Yamaguchi, H. A. Chen, I. Chen, C. W. Chen and M. Chhowalla, *Adv. Mater.*, 2010, **22**, 505–509.
80 Y. Gao, F. Hou, S. Hu, B. Wu, Y. Wang, H. Zhang, B. Jiang and H. Fu, *ChemCatChem*, 2018, **10**, 1330–1335.
81 Q. Mei, K. Zhang, G. Guan, B. Liu, S. Wang and Z. Zhang, *Chem. Commun.*, 2010, **46**, 7319–7321.
82 D. Qu, Z. Sun, M. Zheng, J. Li, Y. Zhang, G. Zhang, H. Zhao, X. Liu and Z. Xie, *Adv. Opt. Mater.*, 2015, **3**, 360–367.
83 L. Li, W. Fang, P. Zhang, J. Bi, Y. He, J. Wang and W. Su, *J. Mater. Chem. A*, 2016, **4**, 12402–12406.
84 L. C. Chen, Y. K. Xiao, N. J. Ke, C. Y. Shih, T. F. Yeh, Y. L. Lee and H. Teng, *J. Mater. Chem. A*, 2018, **6**, 18216–18224.
85 H. Tetsuka, R. Asahi, A. Nagoya, K. Okamoto, I. Tajima, R. Ohta and A. Okamoto, *Adv. Mater.*, 2012, **24**, 5333–5338.
86 J. G. Hauge, *J. Biol. Chem.*, 1964, **239**, 3630–3639.
87 S. Q. Peng, Y. J. Peng, Y. X. Li and S. B. Li, *Res. Chem. Intermed.*, 2009, **35**, 739.
88 S. Kumar, A. Kumar, A. Bahuguna, V. Sharma and V. Krishnan, *Beilstein J. Nanotechnol.*, 2017, **8**, 1571–1600.
89 C. V. Pham, M. Krueger, M. Eck, S. Weber and E. Erdem, *Appl. Phys. Lett.*, 2014, **104**, 132102.
90 N. J. Bunce, *J. Chem. Educ.*, 1987, **64**, 907.
91 S. Kempe, H. Metz and K. Mäder, *Eur. J. Pharm. Biopharm.*, 2010, **74**, 55–66.
92 W. S. Hummers and R. E. Offeman, *J. Am. Chem. Soc.*, 1958, **80**, 1339.